Spatially Tailored Asymmetric Oxygen Vacancies Induce Nonradiative Recombination for Ultrafast and Stable NO$_2$ Sensing

Yucheng Ou[a], Nana Xu[b]*, Wei Wang[a]*, Haiyang Song[a], Fuwen Wang[c], Tao Liu[c], Bing Wang[c]*, Ming Zhang[d], Lei Liao[d], Qingjiang Li[a]*

[a]*College of Electronic Science and Technology, National University of Defense Technology, Changsha 410073, China*

[b]*School of Materials Science and Engineering, Hunan University of Science and Technology, Xiangtan 411201, China*

[c]*Science and Technology on Advanced Ceramic Fiber and Composites Laboratory, College of Aerospace Science and Engineering, National University of Defense Technology, Changsha 410073, China*

[d]*Changsha Semiconductor Technology and Application Innovation Research Institute, College of Semiconductors (College of Integrated Circuits), Hunan University, Changsha, China.*

Contents

Experimental Section

Methods

Chemicals and Materials.

Cerous nitrate hexahydrate (Ce(NO$_3$)$_3$·6H$_2$O, 99.95%) were purchased from Aladdin, sodium hydroxide (NaOH, ≅98%) were purchased from Aladdin. The water used in all experiments was ultrapure (18.2 Ω/cm).

Fabrication and testing of a gas sensor and experimental detail.

5 mg of samples are mixed with 50 μL of deionized water to obtain the corresponding slurry. 5 μL of slurry was then dripped on an Pt interdigitated electrodes (10 mm × 5 mm × 0.25 mm, AURORA technologies, China) to form a resistance-type sensor. All the fabricated sensors were aged in air at 80 °C for 2 h. The gas-sensing performance of the fabricated sensors was evaluated using an intelligent gas-sensing analysis system (CGS-4TPs, Beijing Elite Tech Co., Ltd.). To produce test gases with the necessary concentrations, a dynamic gas and liquid distribution system (DGL-III, Beijing Elite Tech Co., Ltd, China) having three mass flow controllers was used. We use nitrogen as the carrier gas, and control the gas flow of oxygen and nitrogen to control the different oxygen concentrations in the reaction chamber. The interference gas is injected into the reaction chamber through a syringe. The room where the gas-sensitive analysis system is located is equipped with a constant temperature and humidity air conditioning system, and the indoor humidity can be artificially controlled by setting parameters. The response value (S_g) is defined as the ratio of resistance in air (R_a) to resistance in target gas (R_g). The response time and recovery

time are defined as the time for the sensor to reach 90% of the final signal.

Characterization and measurements. X-ray diffraction (XRD) patterns were recorded on a Bruker D8 X-ray powder diffractometer with Cu Kα radiation (λ = 1.5418 Å) at 30 kV and 10 mA with a scanning rate of 5° min^{-1} in the 2θ range of 10° ~ 80°. The HRTEM images were taken on a Talos F200i working at 200 kV and JEOL JEM-2100F field emission transmission electron microscopy with an accelerating voltage of 200 kV. The high-angle annular dark-field scanning transmission electron microscopy (HAADF-STEM) images and Xray energy dispersive spectroscopy (EDS) mapping was recorded on aberration-corrected TEM (FEI Titan Cubed Themis G2 300) at an accelerating voltage of 300 kV. Si (Li) EDS detector with a solid angle of 0.13 srad and Fiori number > 4000. 1.85 s/pixel and gather a 460 pixel map, so the time of EDS acquisition will cost 851 seconds. The In situ Fourier-transform infrared (In situ FT-IR) spectra were recorded on a Bruker Vertex 70 FTIR spectrometer equipped with in situ reaction chamber. X-band electron paramagnetic resonance (EPR) measurement was performed at room temperature using a JEOL FA-200 EPR spectrometer. The X-ray photoelectron spectroscopy (Axis Supra) measurements were operated with Al Ka radiation (1486.6 eV). Binding energies (BE) were calibrated by setting the measured BE of C 1s to 284.8 eV. In situ DRIFTS spectra were measured on a Nicolet-6700 FTIR spectrometer. The N_2 adsorption-desorption isotherms were measured using a BELSORP-max-II to estimate specific surface area and pore size distribution by the Brunauer-Emmett-Teller (BET) and Barrett–Joyner–Halenda (BJH) methods. The process Raman system employed in

this study was HORIBA. X-ray absorption fine spectra (XAFS) measurements were measured on the B11 station in Shanghai Synchrotron Radiation Facility (SSRF). The KPFM (Bruker MultiMode-8 surface potential mode) was used to characterize the surface potential. The SCM-PIT-V2 model tip and AS-130VLR ("J" vertical) scanner model was used, and the radius and elastic coefficient of tip were 35 nm and 3 N/m, respectively. A 300 W Xe arc lamp irradiated at the sample to provide the light condition. In this study, the samples were coated on highly oriented pyrolytic graphite substrate. All the KPFM measurement was carried out at ambient conditions. The contact potential difference (CPD) was defined as the difference between the work function of the tip and the sample. The images were processed by first order flattening to eliminate errors caused by sample tilt. The Fluoromax-4 spectrophotometer (HORIBA Scientific, excited at λ=325 nm) given the photoluminescence spectra (PL).

X-ray absorption data analysis

The obtained XAFS data was processed in Athena (version 0.9.26) for background, pre-edge line and post-edge line calibrations. Then Fourier transformed fitting was carried out in Artemis (version 0.9.26). The k2 weighting, k-range of 2-10 $Å^{-1}$ and R range of 1-3 Å were used for the fitting of CeO_2 and Sample.

DFT calculations.

DFT calculations are carried out using the VASP code. The projector augmented-wave (PAW) method and Perdew-Burke-Ernzerhof generalized gradient approximation (GGA-PBE) ae used for the exchange correlation functionals. The energy cutoff of 400 eV is used. The molecular dynamics simulations are carried out in the canonical

ensemble (NVT) with the Nose-Hoover thermostat. The time step is set to 1 fs. All initial amorphous structures are thermally equilibrated at ambient temperature for 25 ps. The energy and force on each ion are reduced below 10^{-5} eV/atom and 0.01 eV/A, respectively, and only the Γ point was sampled from the Brillouin zone. The amorphous models were obtained by using the heat up process: from 0 to 900 K within 25 ps to obtain the structural snapshots and total energy distributions at the corresponding temperatures. The effect of core electrons on the density of valence electrons was described using the projector augmented wave method. The kinetic energy cutoff for the plane waves was set to 450 eV for all the calculations. To consider the open-shell d-electrons, GGA+U schemes were implemented, employing effective U values of 5.0 for Ce. The convergence tolerance of energy and force on each atom during structure relaxation were less than 10^{-5} eV and 0.03 eV/Å, respectively. A set of Monkhorst–Pack mesh K points of 2×2×1 and 4×4×1 is used to sample the Brillouin zone for geometry optimization and electronic structural calculations. A vacuum distance of 15 Å was set to ensure sufficient vacuum and avoid interactions between two periods. Further calculations were carried out to determine the thermal and zero-point energy (ZPE) corrections at the Γ point of various intermediates adsorbed on the surface. The VASPKIT code was used for postprocessing computational data obtained from VASP.

The adsorption energy can be evaluated by ΔG_{ads}, which is defined as

$$\Delta E_{ads} = E_{(System+\ gas)} - E_{(System)} - 1/2\ E_{ads},$$

in which $E_{(System+\ gas)}$ and $E_{(System)}$ are the energies of all research systems with and

without gas adsorption, respectively. Eads represents the energy of adsorbed intermediates.

II. Supplementary Figure
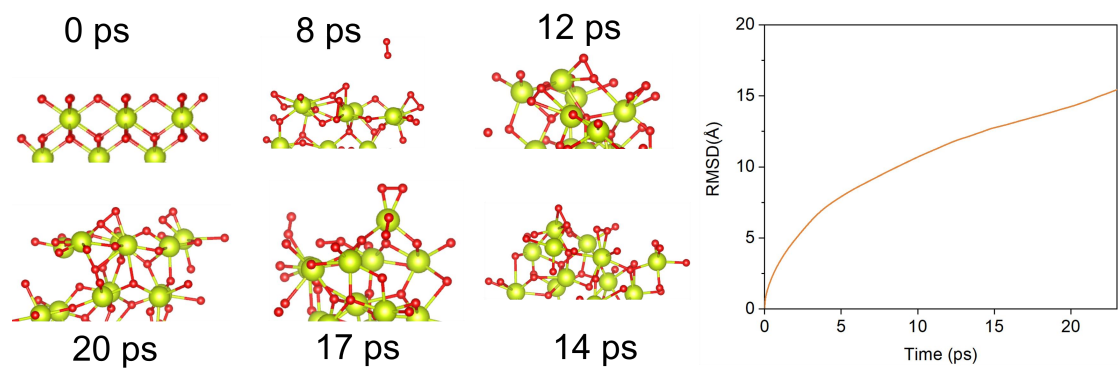
Fig. S1. MD analysis of CeO_2.
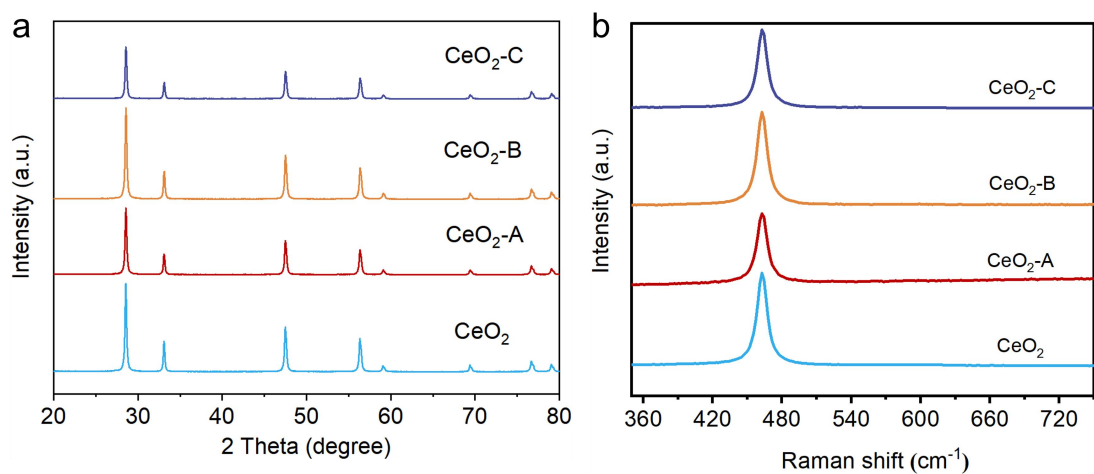
Fig. S2. a XRD pattern of CeO_2, CeO_2-A, CeO_2-B and CeO_2-C. b Raman spectra of CeO_2, CeO_2-A, CeO_2-B and CeO_2-C.
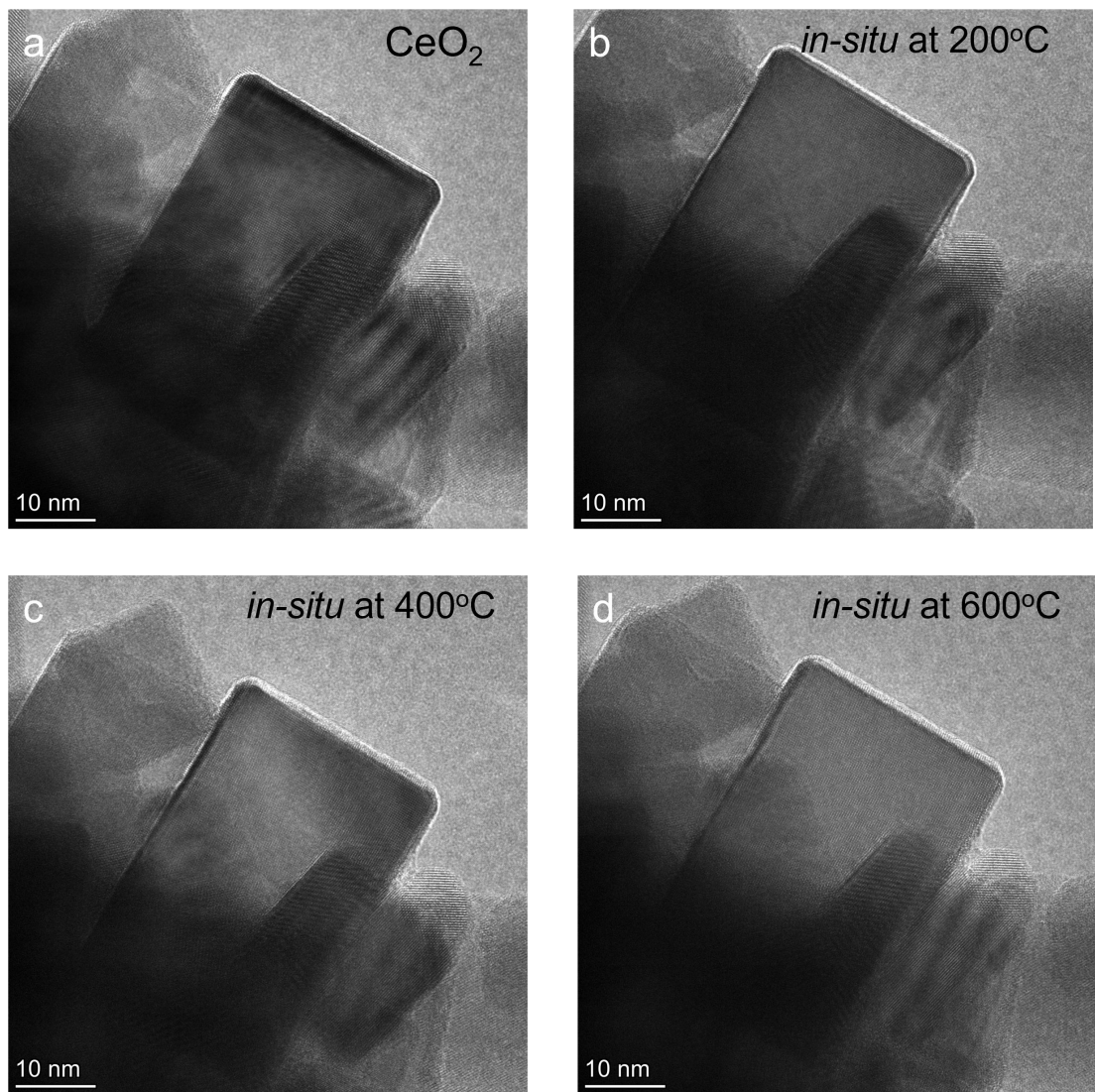
Fig. S3. *In-situ* analysis of CeO_2.
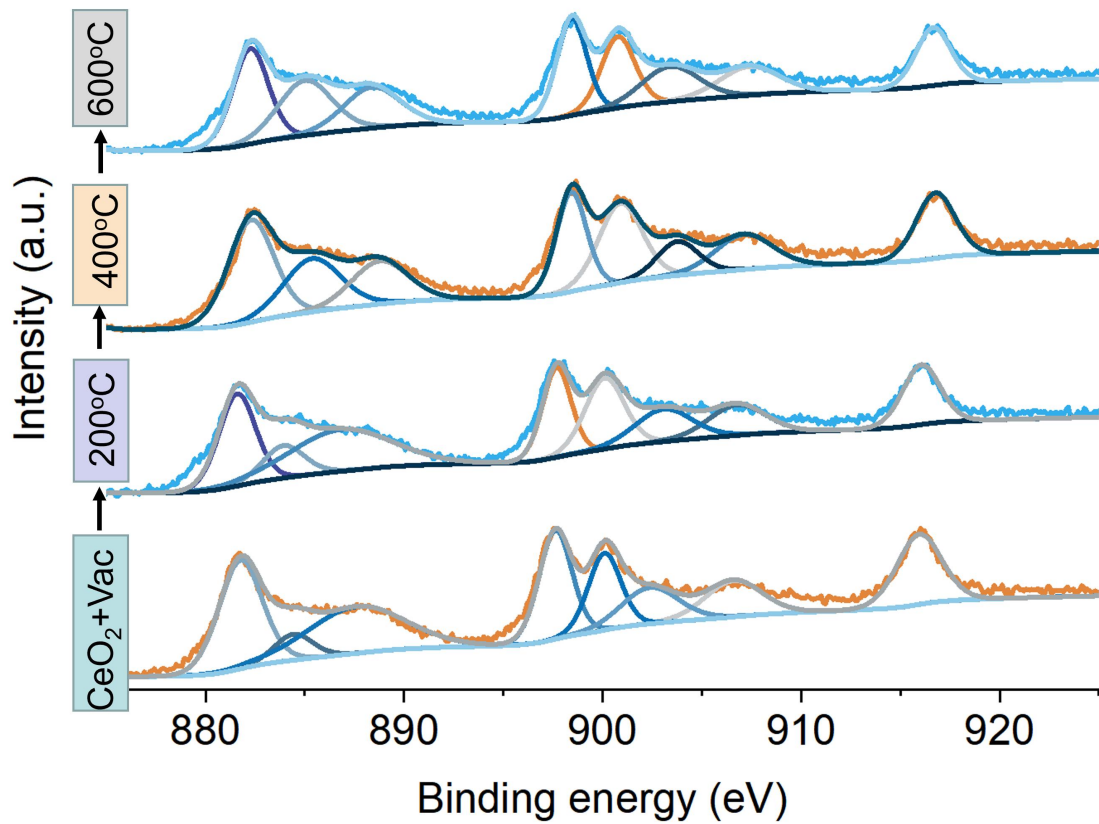
Fig. S4. *In-situ* NAP-XPS analysis of CeO$_2$.
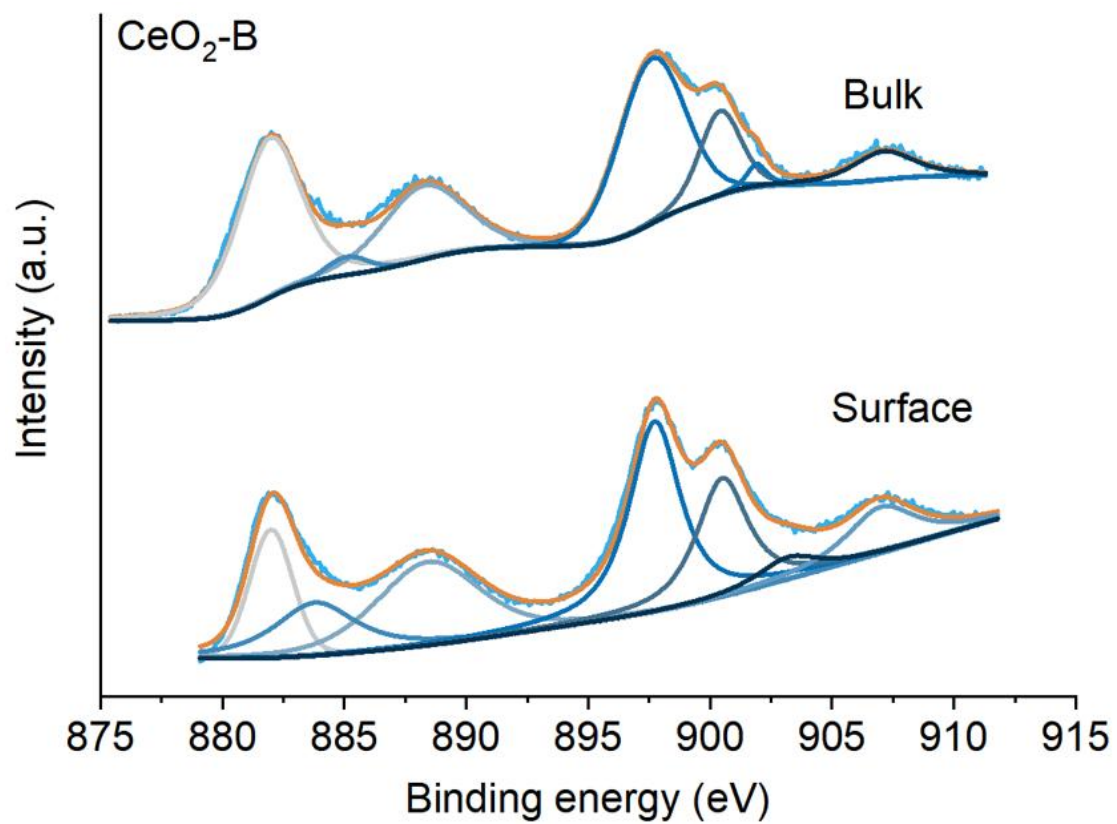
Fig. S5. HAXPES analysis of CeO$_2$-B.
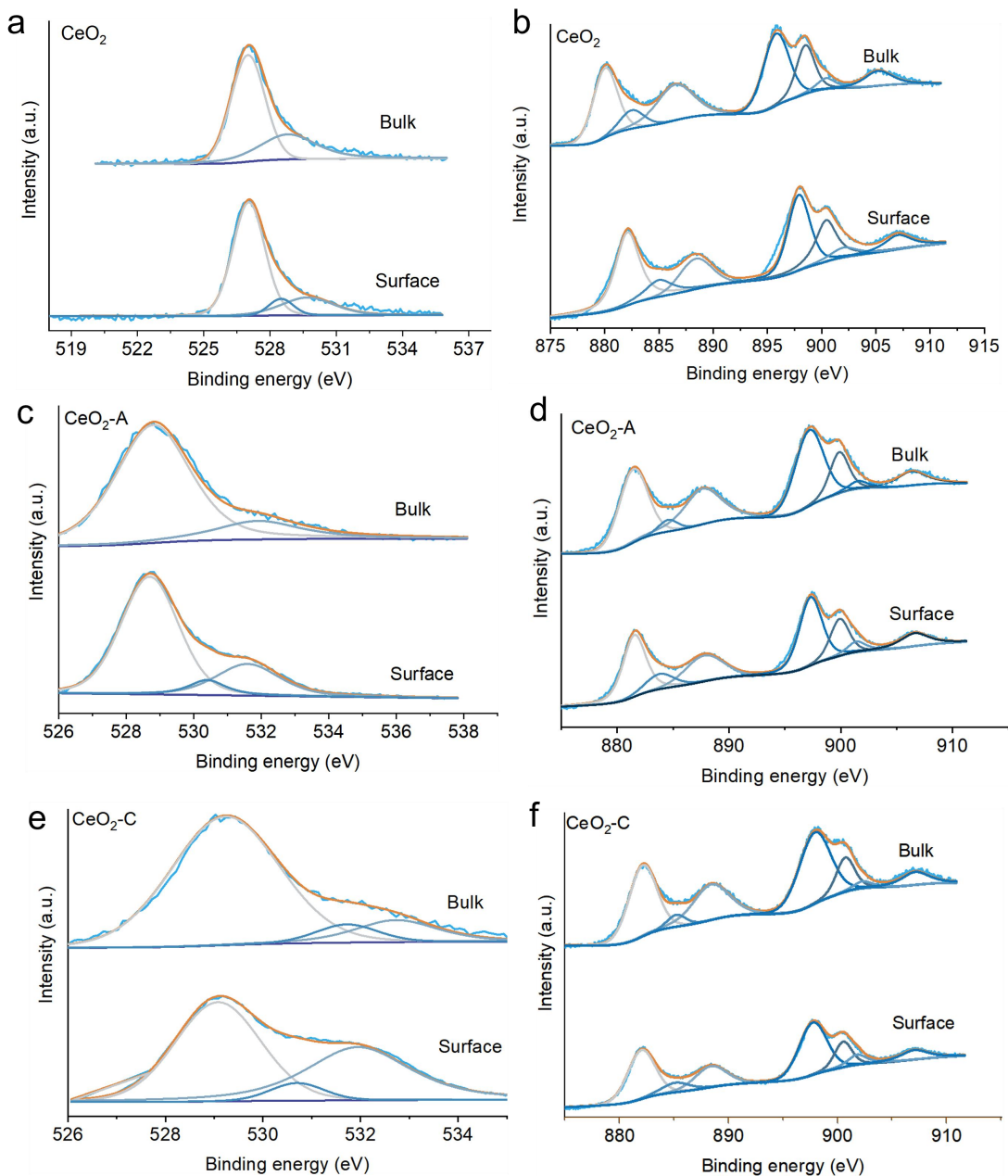
Fig. S6. a-b HAXPES analysis of CeO_2. c-d HAXPES analysis of CeO_2-A. e-f HAXPES analysis of CeO_2-C.
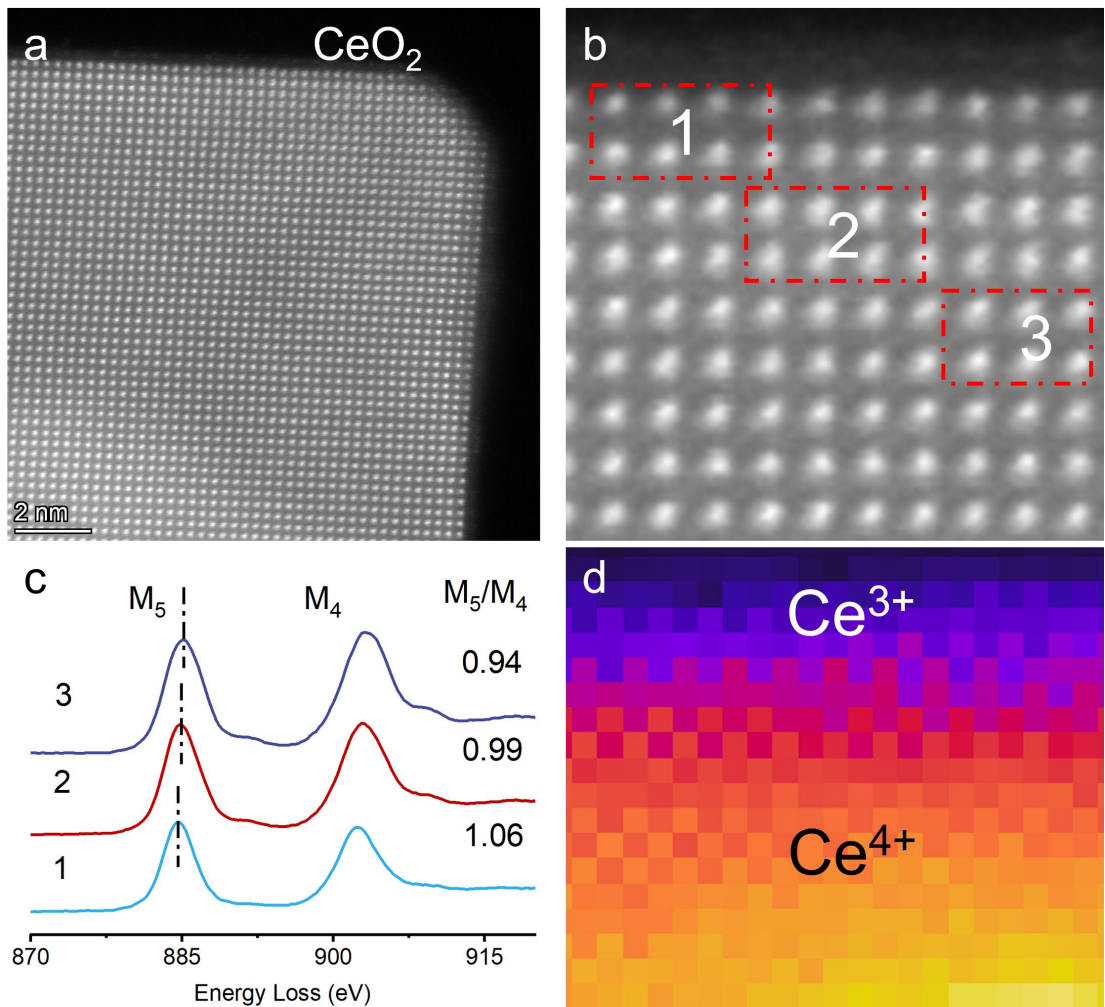
Fig. S7. AC-TEM of CeO_2.
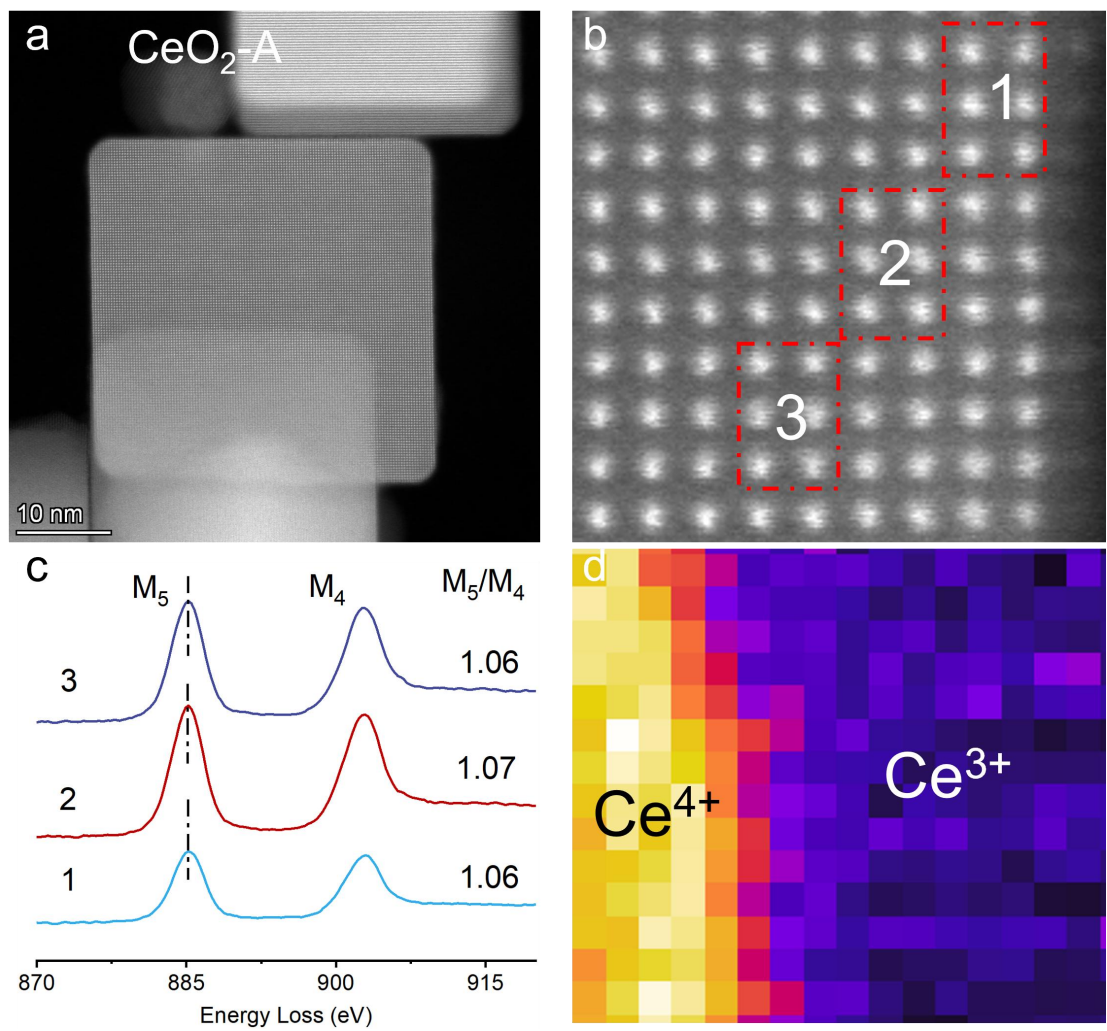
Fig. S8. AC-TEM of CeO$_2$-A.
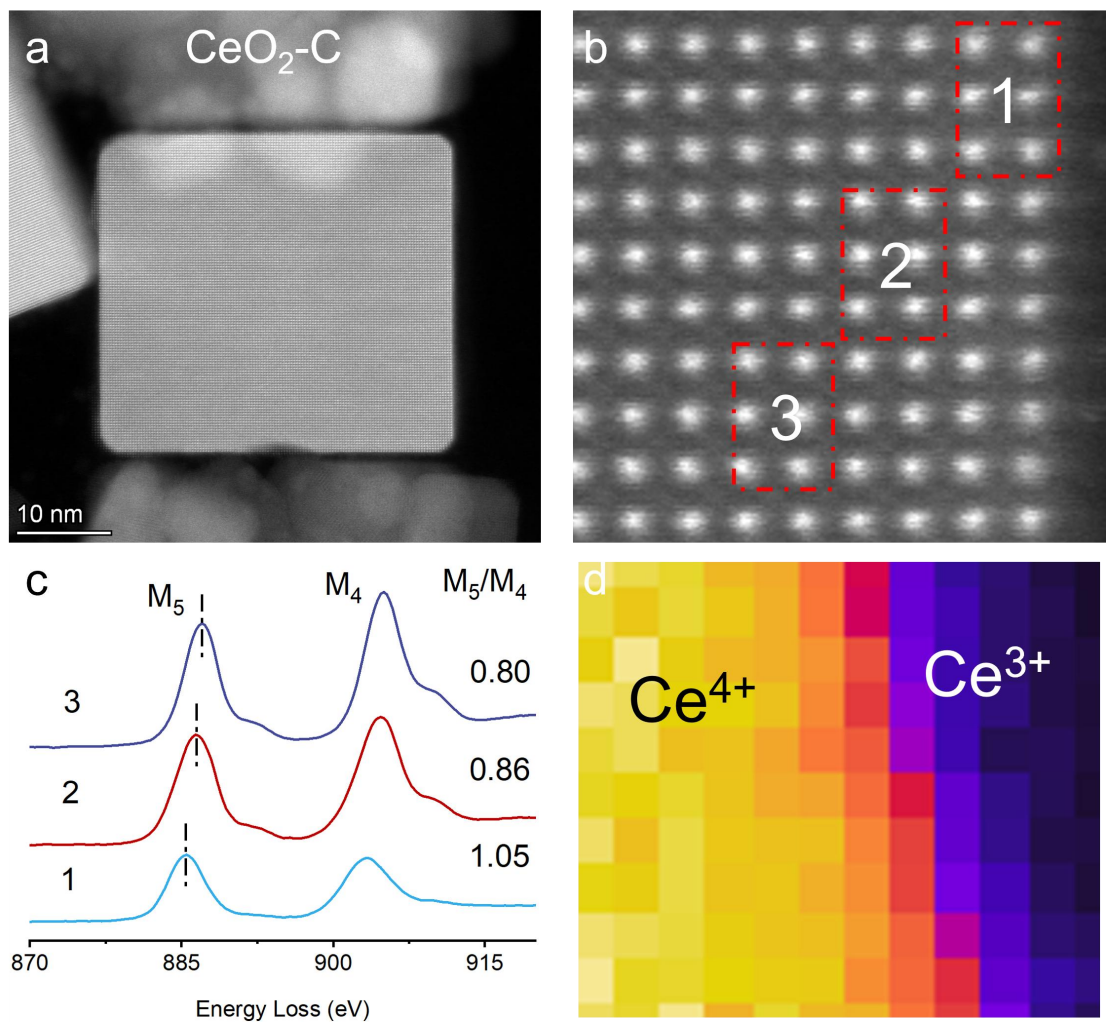
Fig. S9. AC-TEM of CeO$_2$-C.
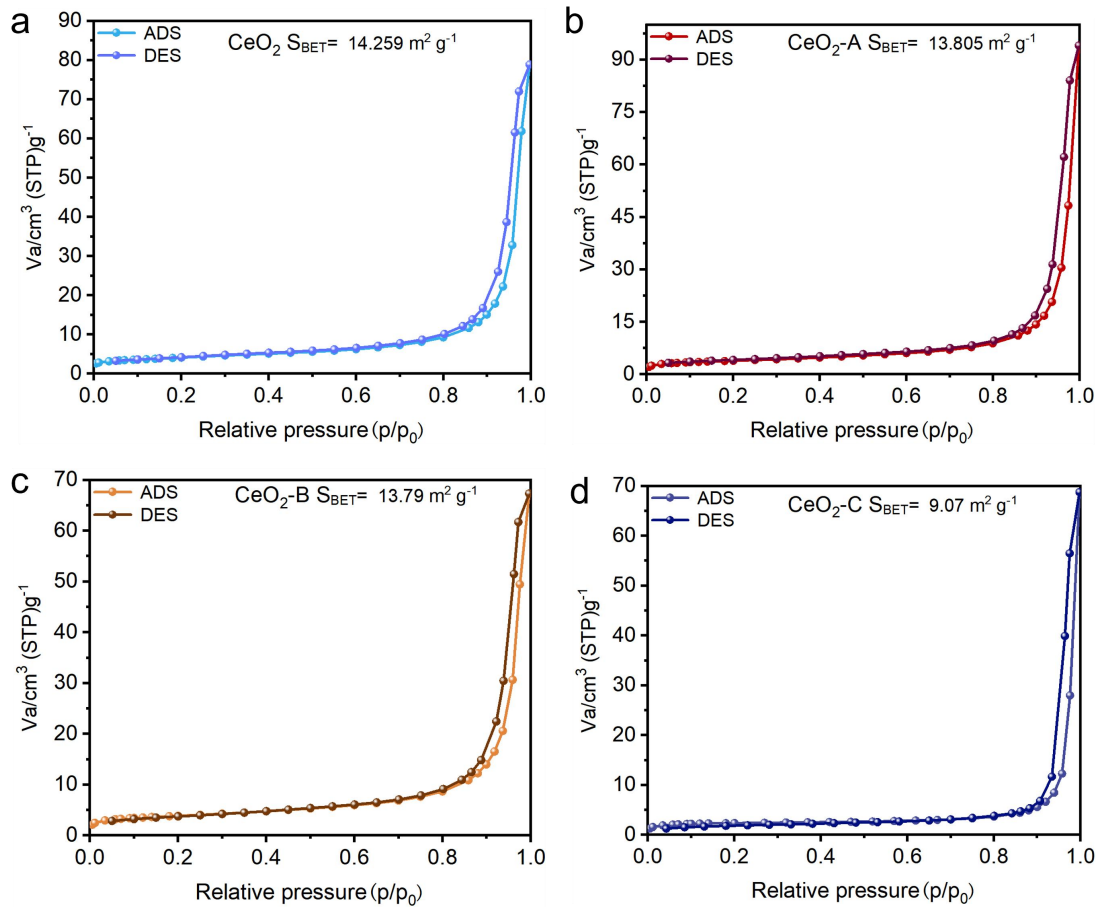
Fig. S10. BET of CeO$_2$, CeO$_2$-A, CeO$_2$-B and CeO$_2$-C.
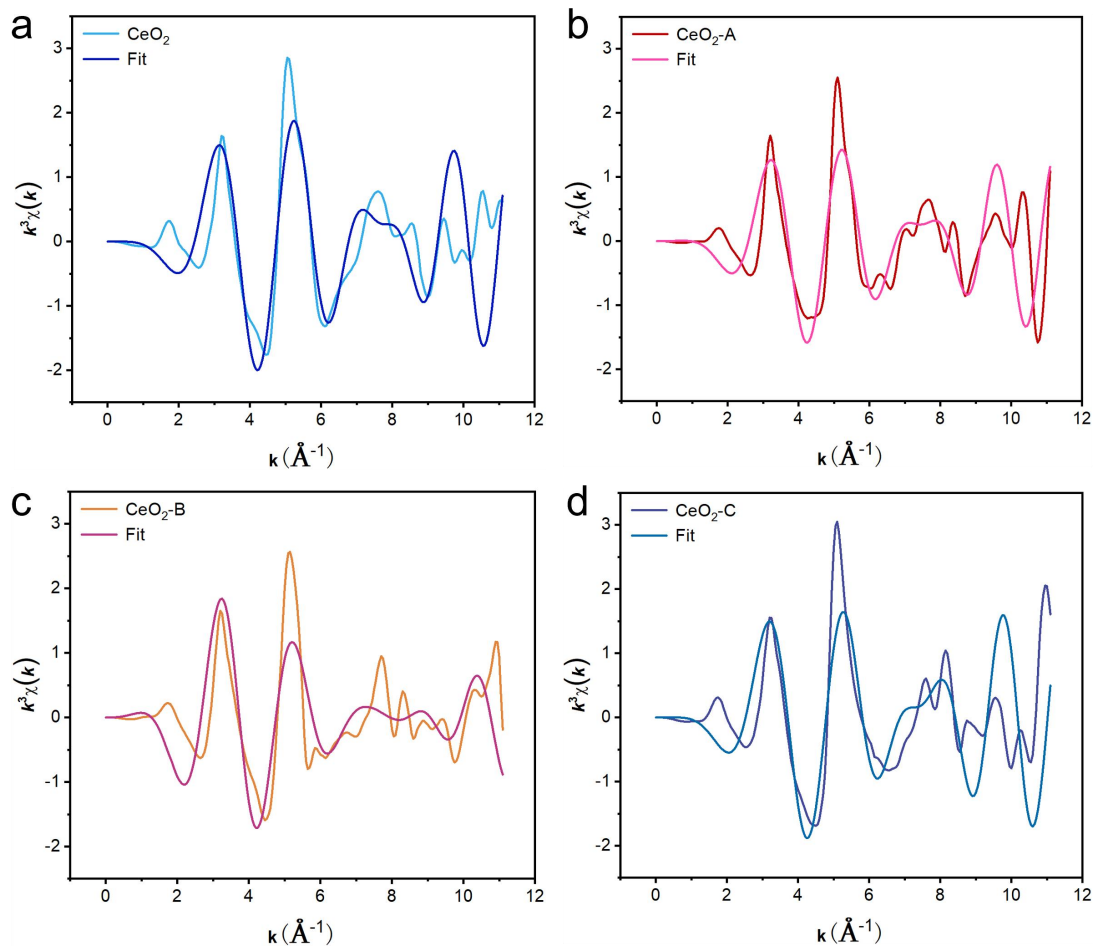
Fig. S11. Experimental and fitting results of Fourier transformed extended X-ray absorption fine structure (EXAFS) spectra of CeO_2, CeO_2-A, CeO_2-B and CeO_2-C.
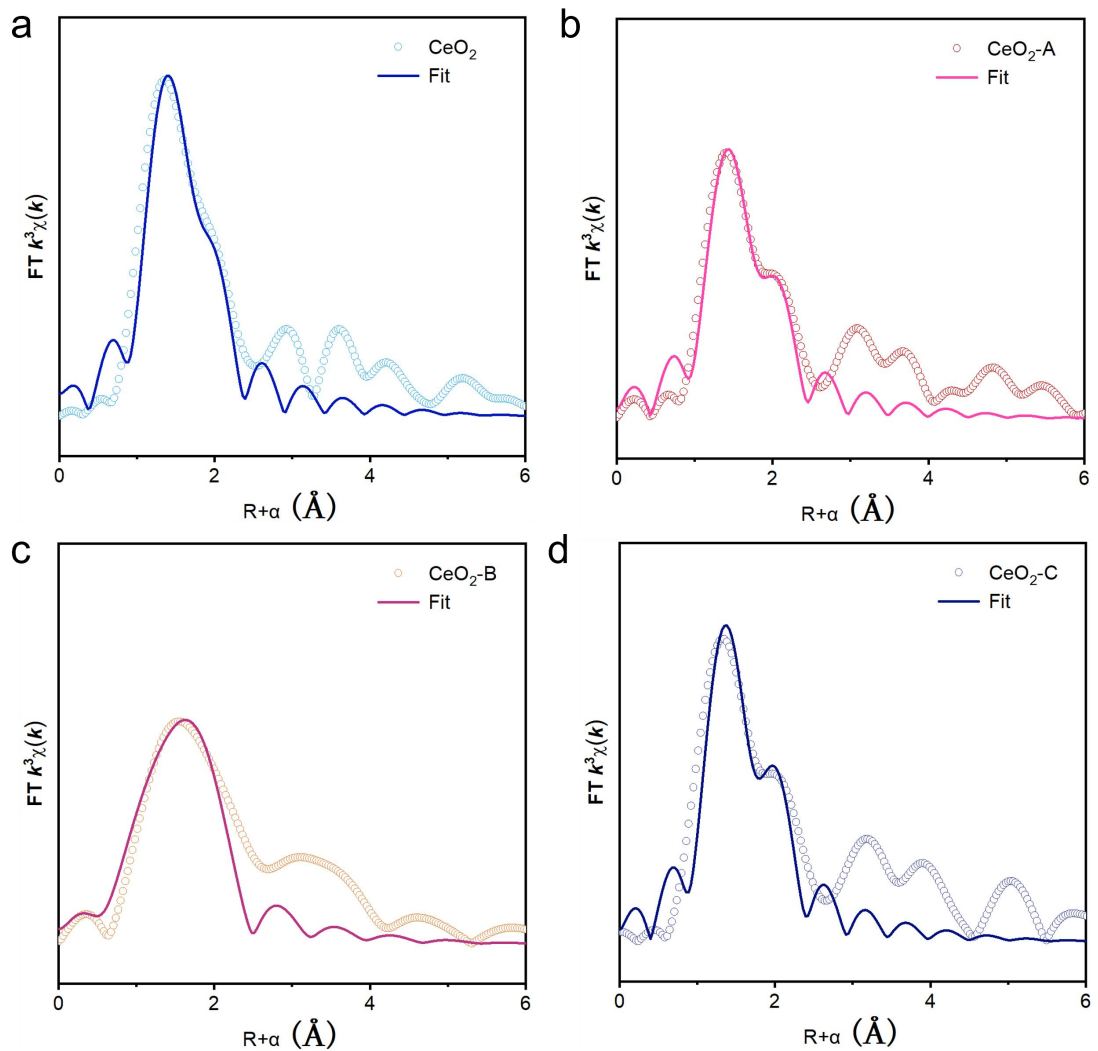
Fig. S12. FT-EXAFS curves at Ce L_3-edge, where the curve is experimental

data and the circle is the best fit for CeO_2, CeO_2-A, CeO_2-B and CeO_2-C.
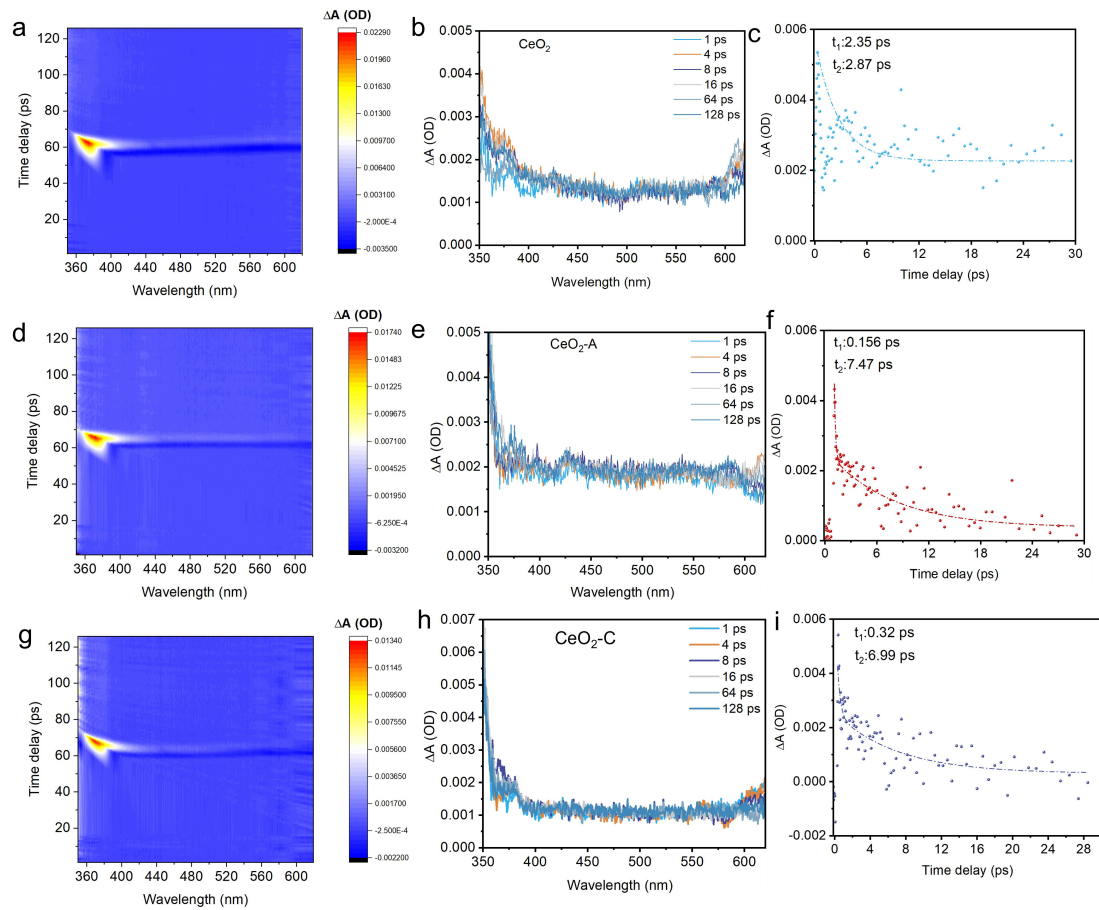
Fig. S13. TA spectra of CeO₂, CeO₂-A and CeO₂-C.
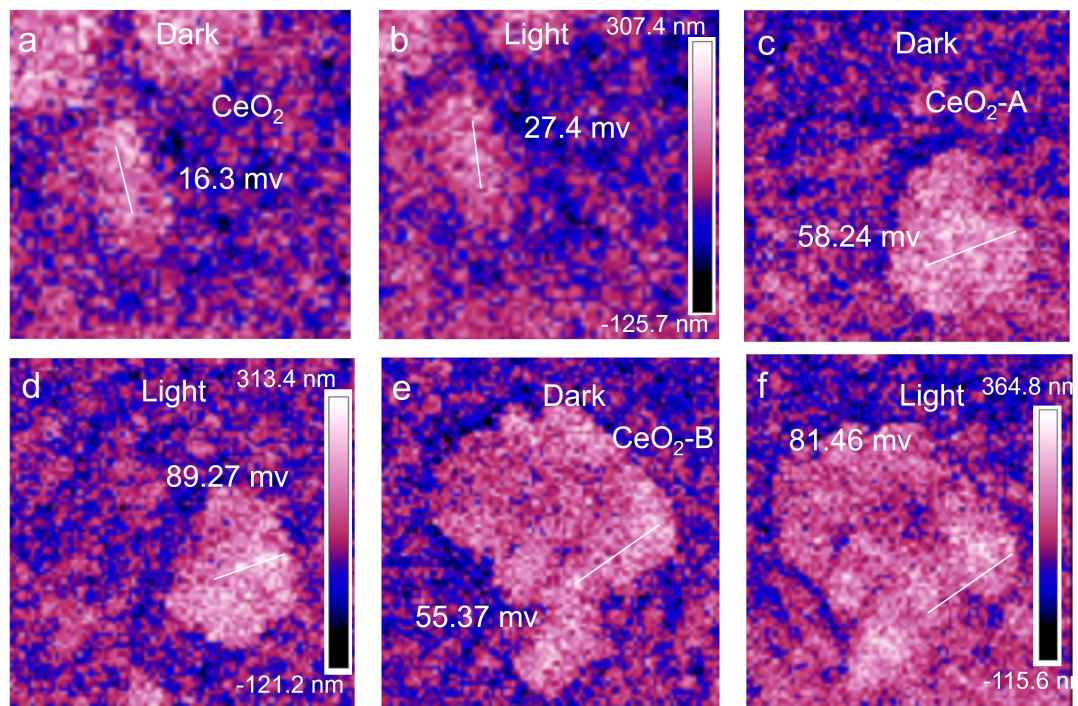
Fig. S14. KPFM image of CeO$_2$, CeO$_2$-A and CeO$_2$-C.
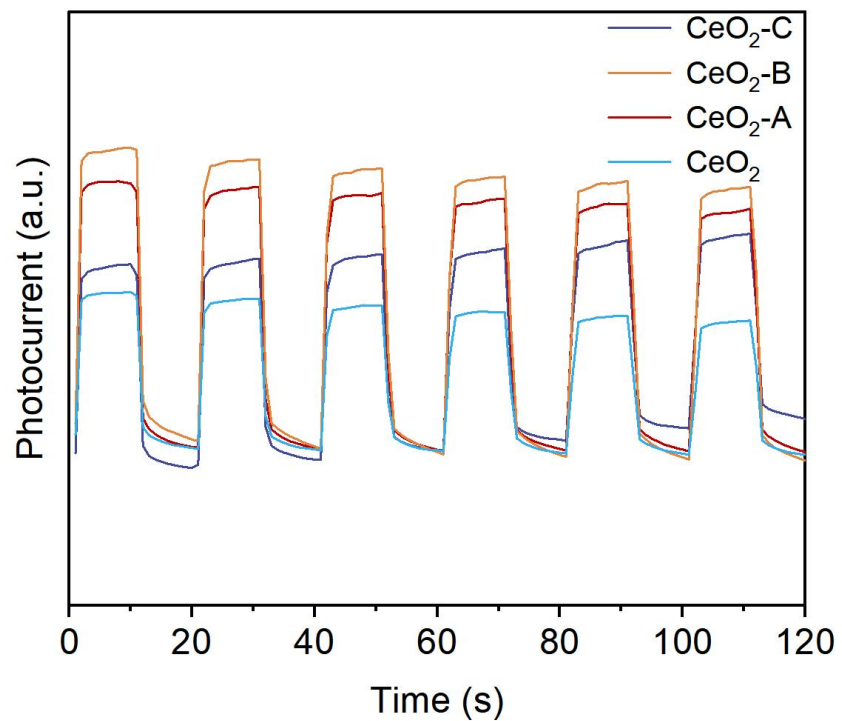
Fig. S15. Photocurrent signal of CeO_2, CeO_2-A, CeO_2-B and CeO_2-C.

a 142.45 µm 250µm

b Ce 250µm
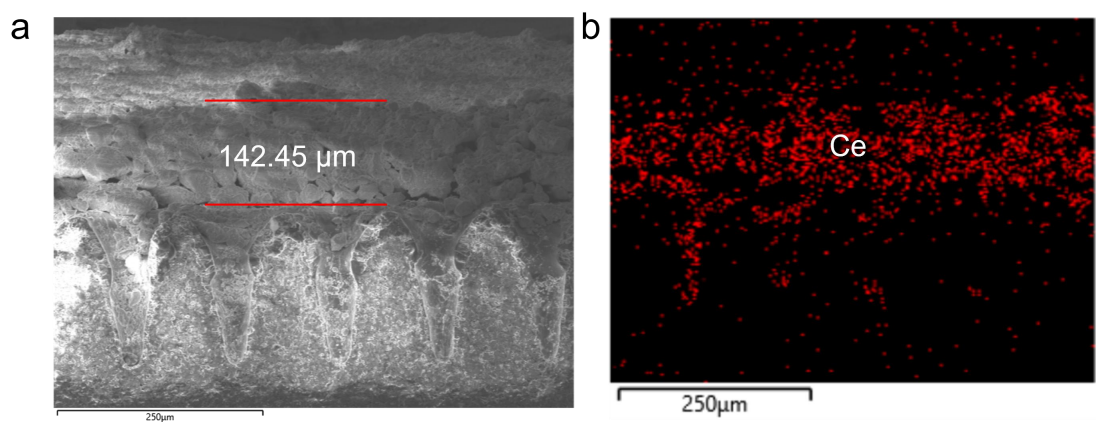
Fig. S16. The thickness of sensing layer.
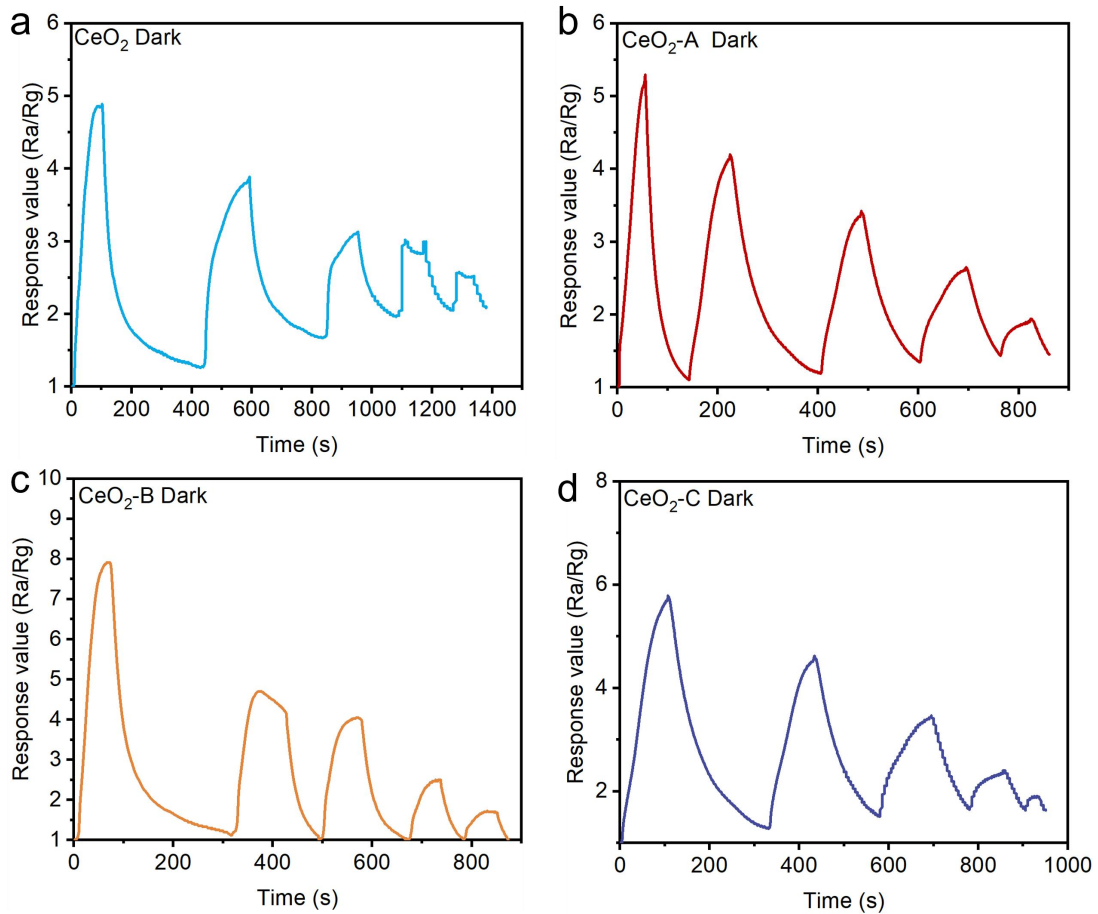
Fig. S17. Response values dynamic curve of CeO$_2$, CeO$_2$-A, CeO$_2$-B and
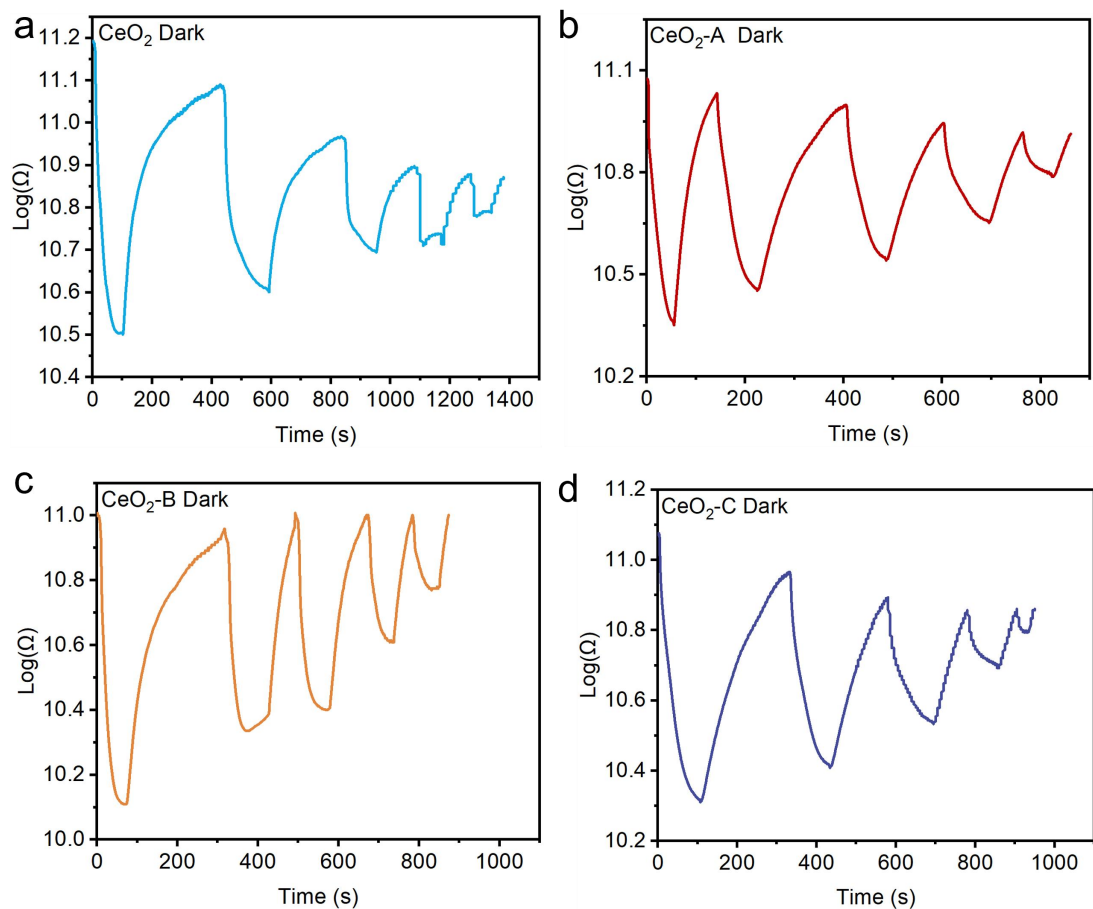
CeO$_2$-C under dark.

Fig. S18. Resistance dynamic curve of CeO_2, CeO_2-A, CeO_2-B and CeO_2-C under dark.
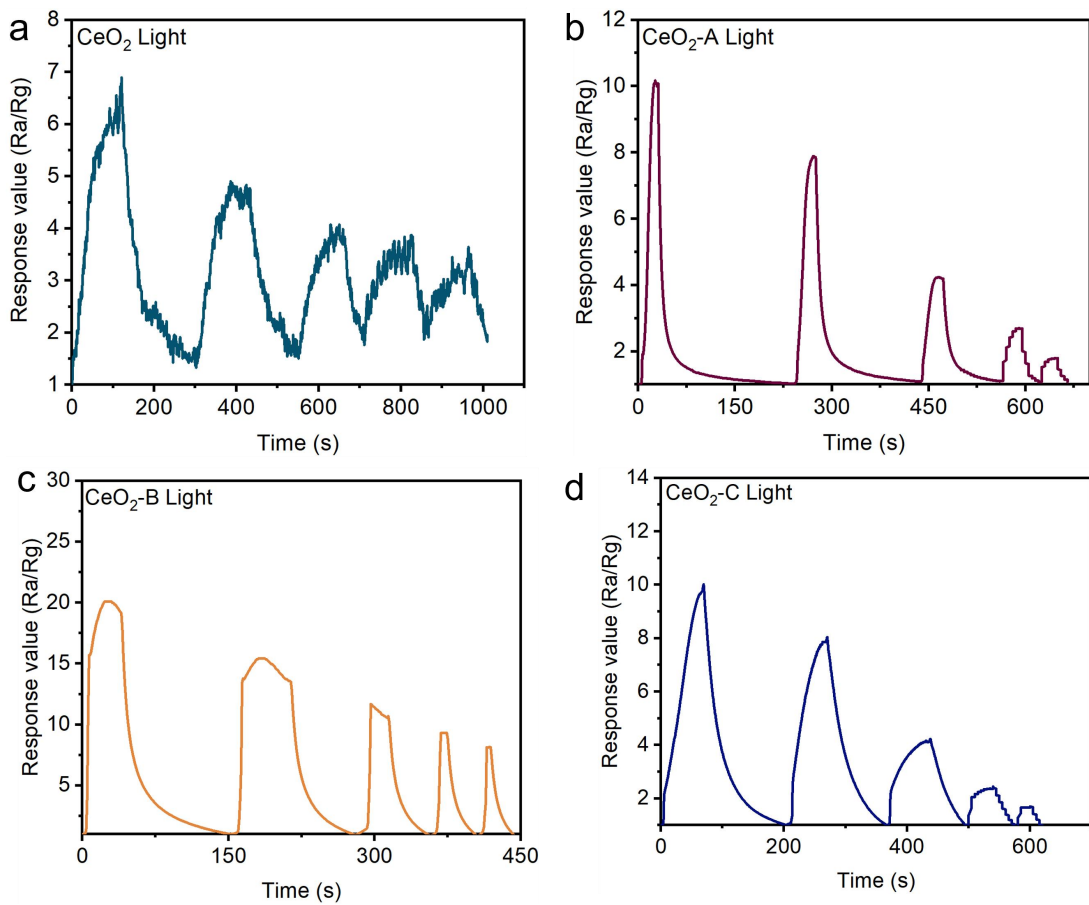
Fig. S19. Response values dynamic curve of CeO_2, CeO_2-A, CeO_2-B and CeO_2-C under light.
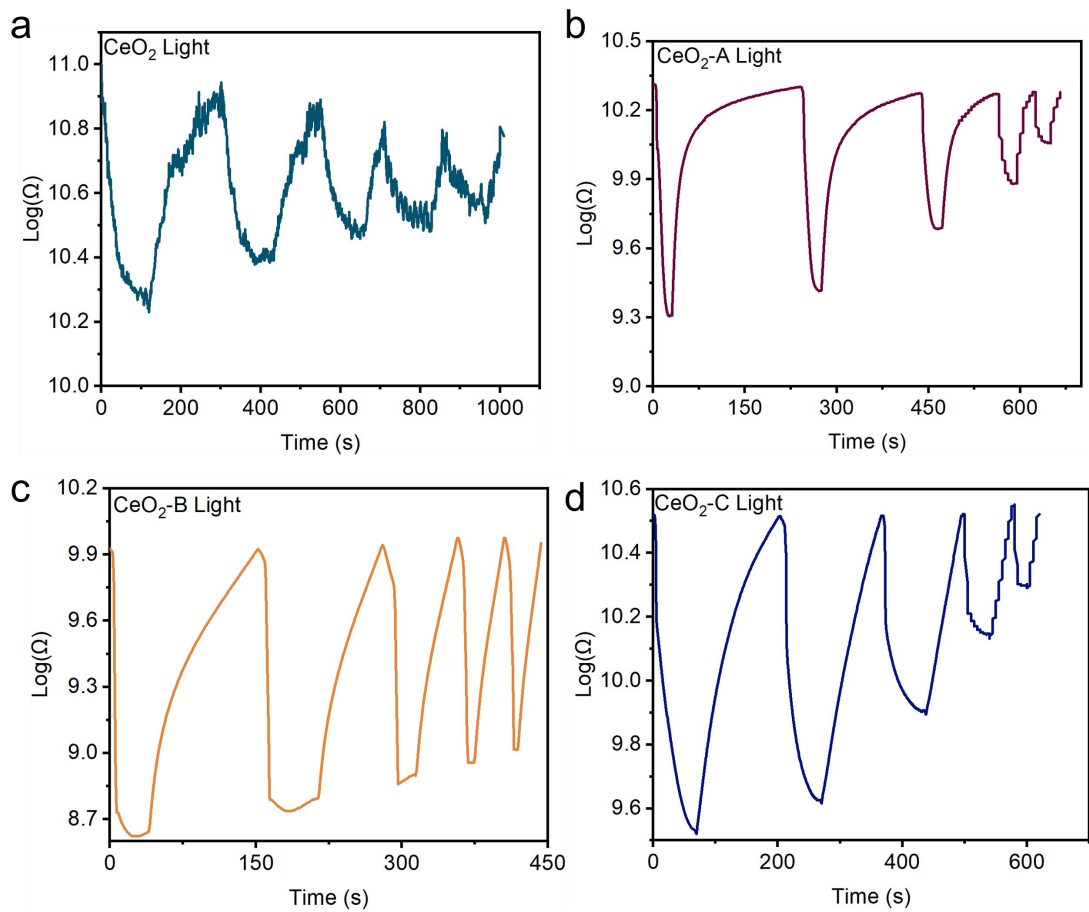
Fig. S20. Resistance dynamic curve of CeO$_2$, CeO$_2$-A, CeO$_2$-B and CeO$_2$-C under light.
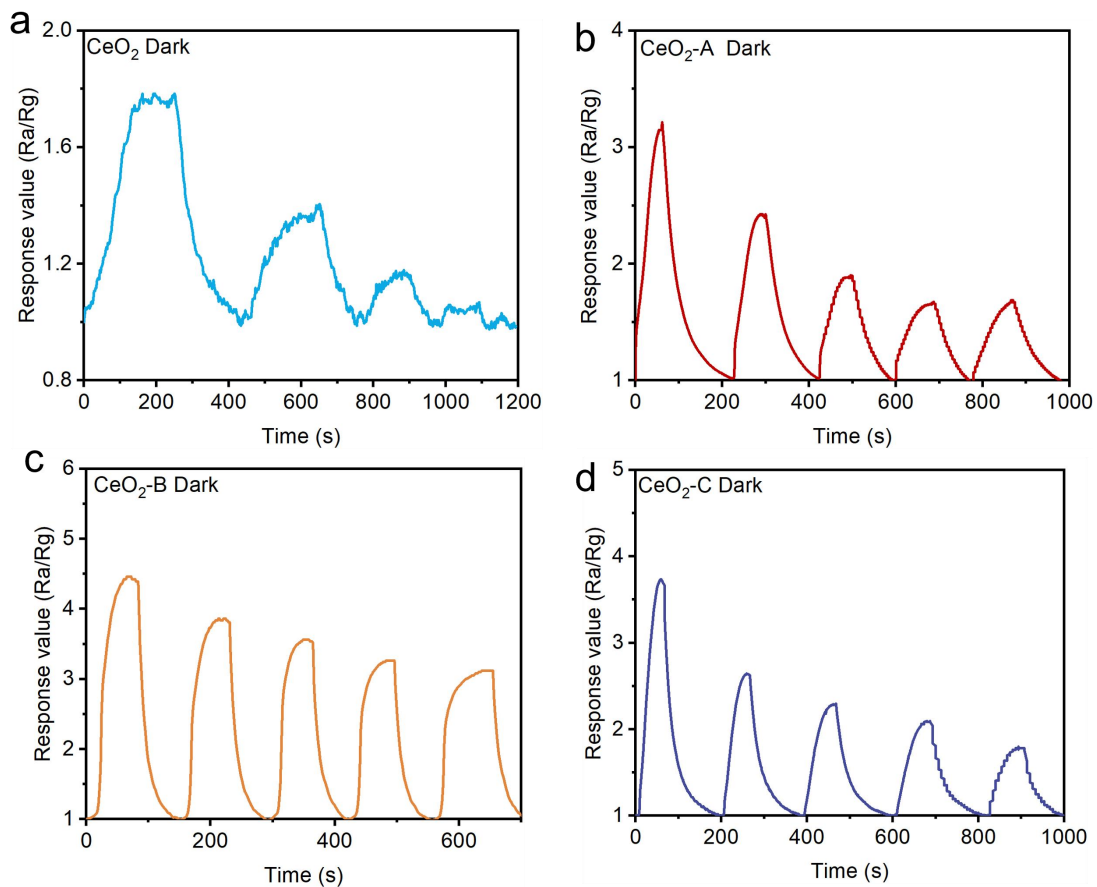
Fig. S21. Response values dynamic stability of CeO$_2$, CeO$_2$-A, CeO$_2$-B and
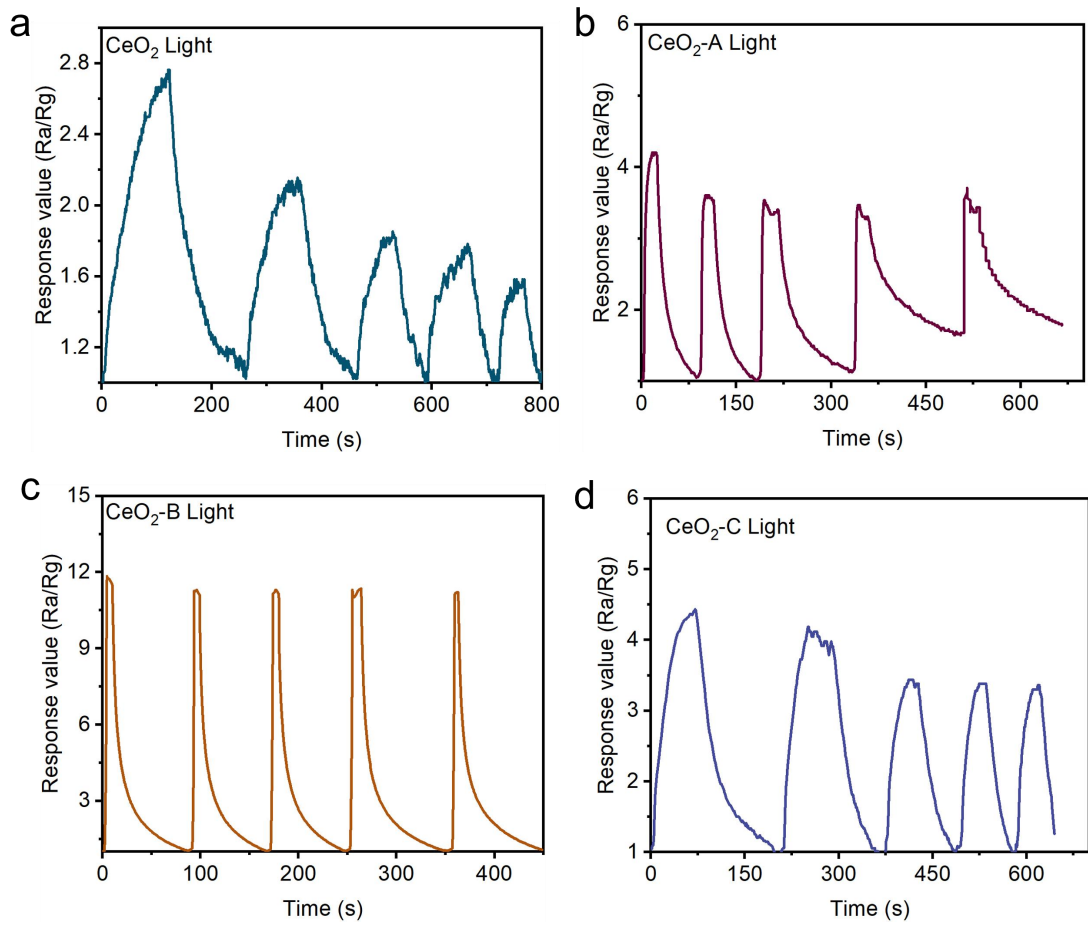
CeO$_2$-C under dark.

**Fig. S22.** Response values dynamic stability of CeO$_2$, CeO$_2$-A, CeO$_2$-B and CeO$_2$-C under light.
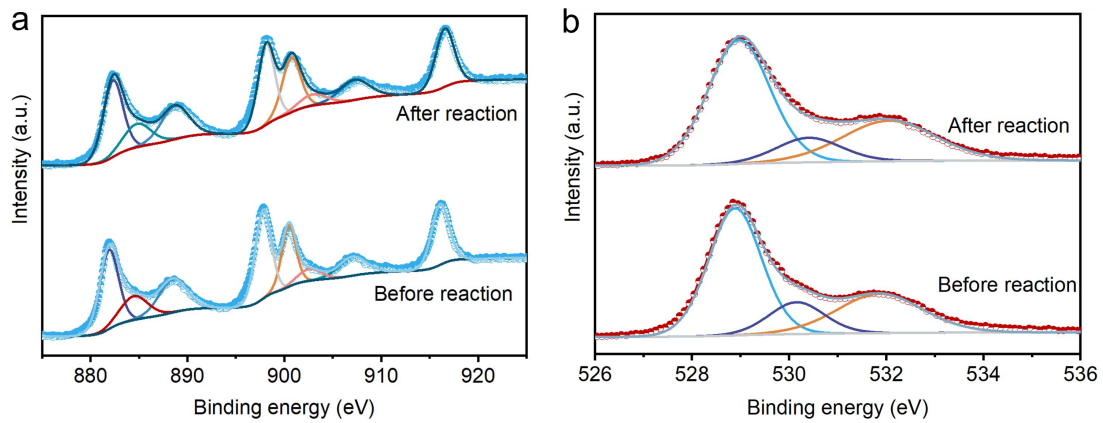
**Fig. S23.** Ce 3d and O2p high-resolution XPS spectra of CeO_2-B after reaction.
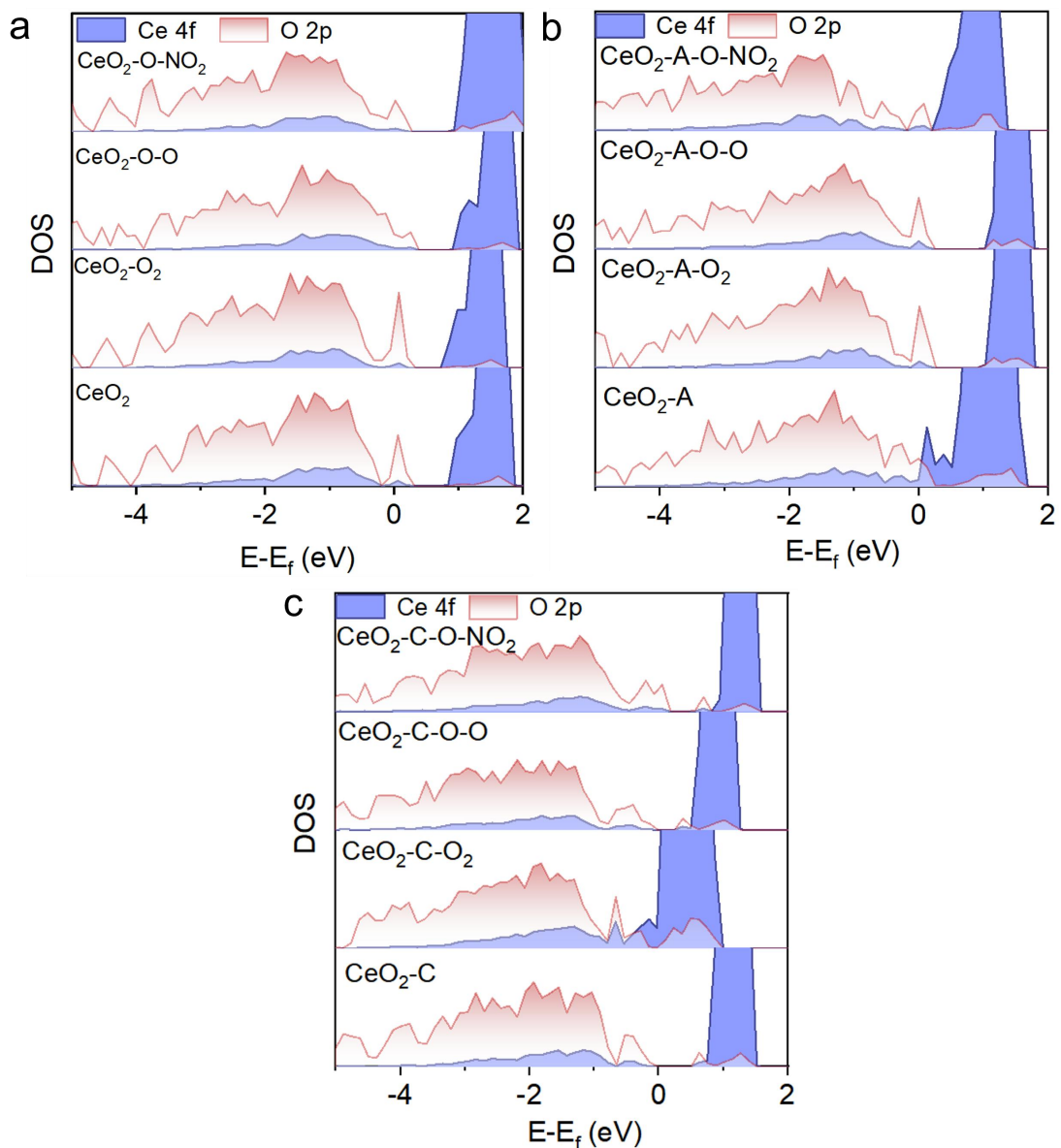
Fig. S24. DOS analysis of CeO_2, CeO_2-A and CeO_2-C.

CeO$_2$
1.225Å   0.12e
E_{ads}=-1.321 eV

CeO$_2$-A
1.239Å   0.21e
E_{ads}=-1.376 eV

CeO$_2$-C
1.244Å   0.18e
E_{ads}=-1.367 eV

CeO$_2$
1.186Å   0.108e
E_{ads}=-0.409 eV

CeO$_2$-A
1.187Å   0.162e
E_{ads}=-1.023 eV

CeO$_2$-C
1.209Å   0.153e
E_{ads}=-0.972 eV
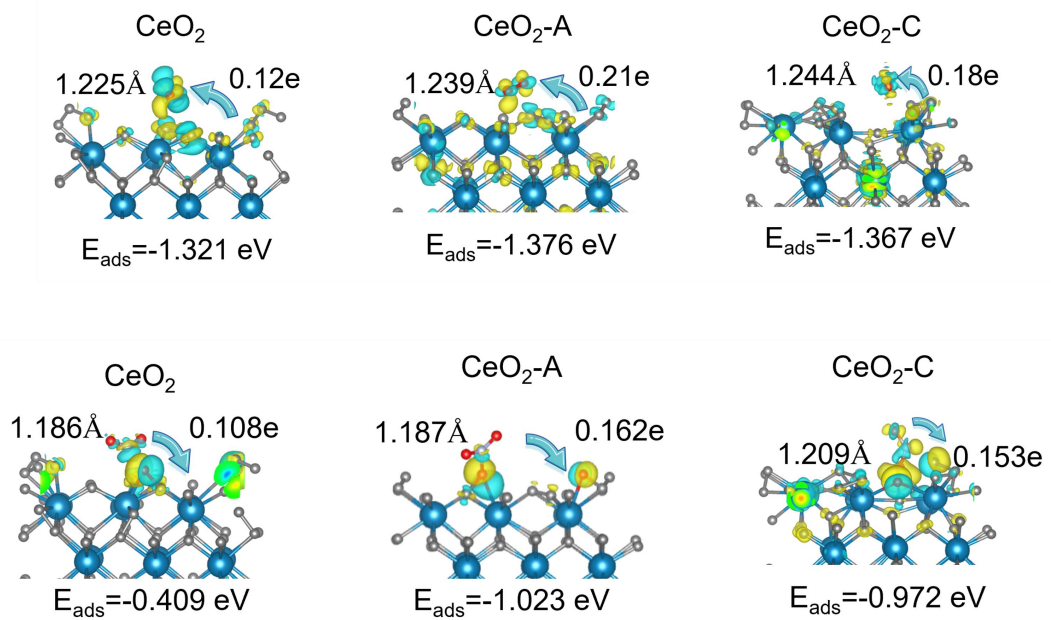
Fig. S25. Adsorption energy of CeO$_2$, CeO$_2$-A and CeO$_2$-C toward O$_2$ and NO$_2$.
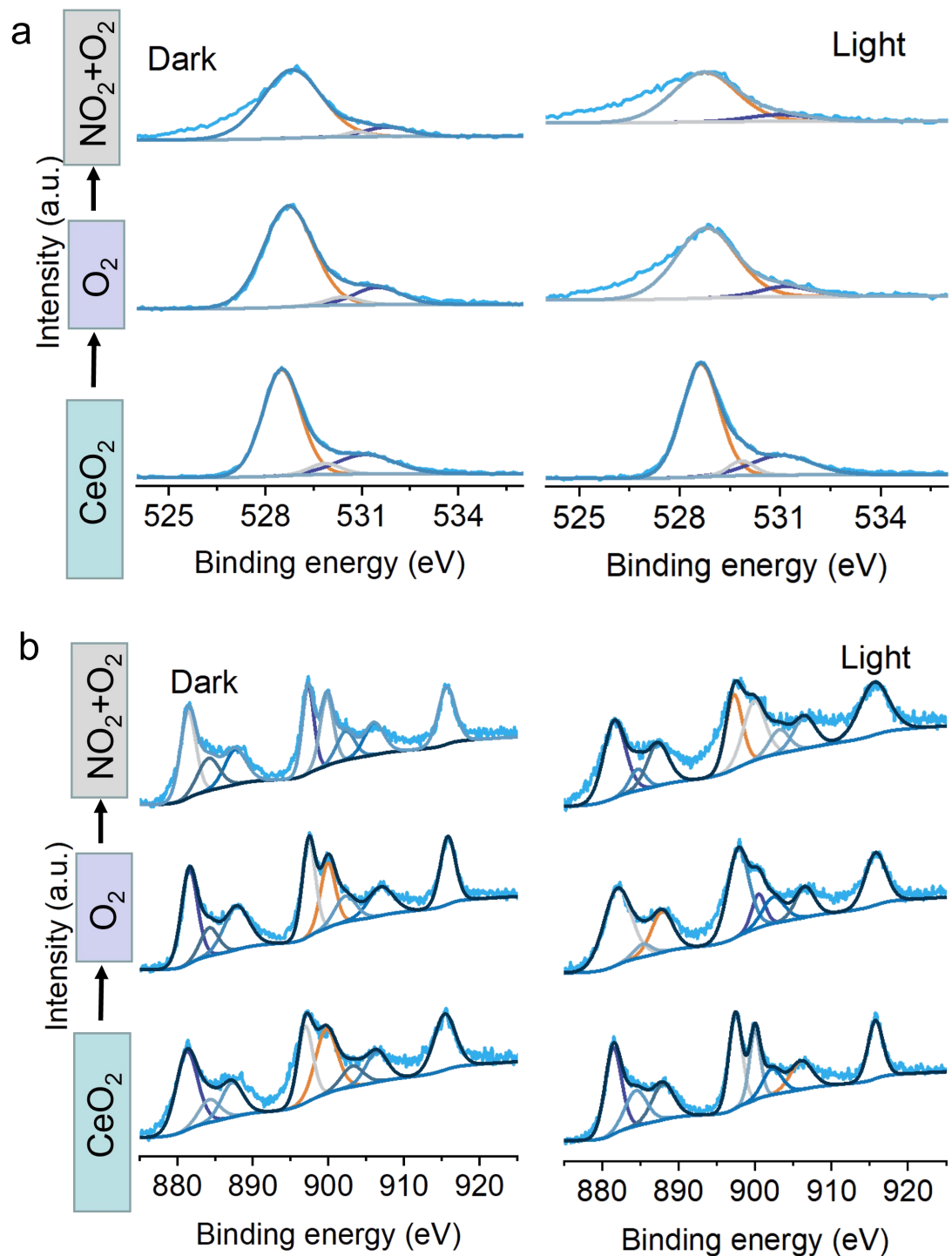
Fig. S26. NAP-XPS analysis of CeO$_2$.
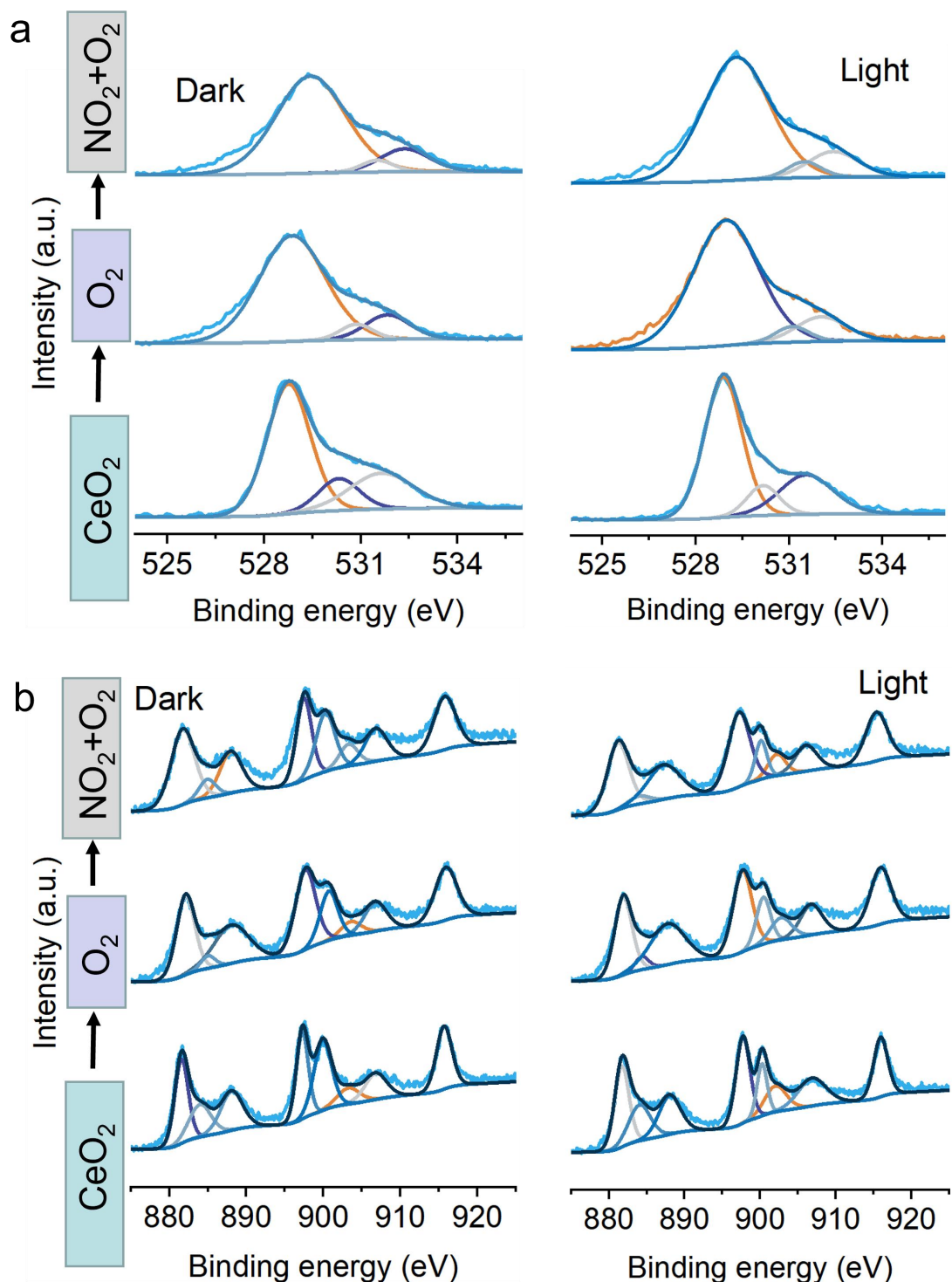
Fig. S27. NAP-XPS analysis of CeO$_2$-A.
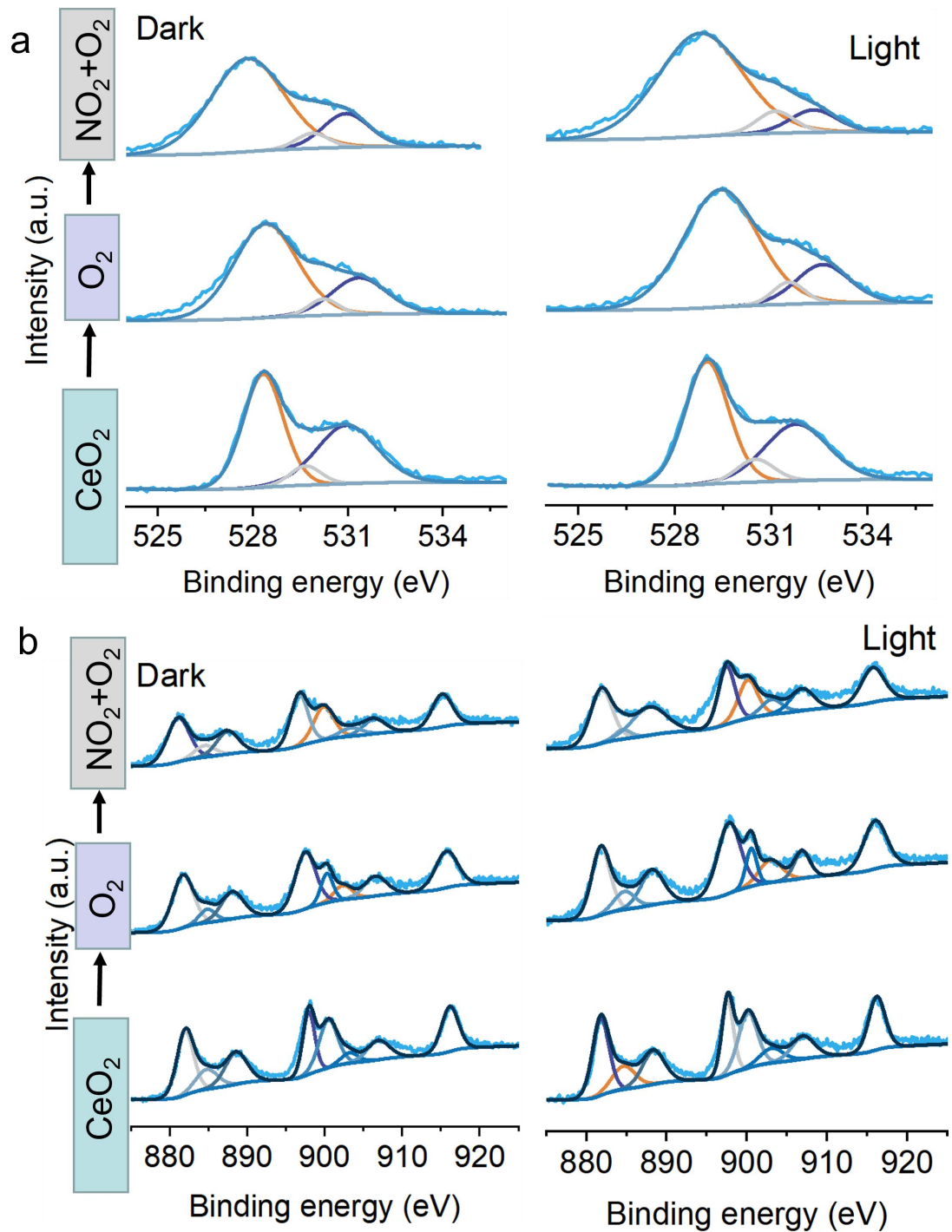
Fig. S28. NAP-XPS analysis of CeO_2-C.
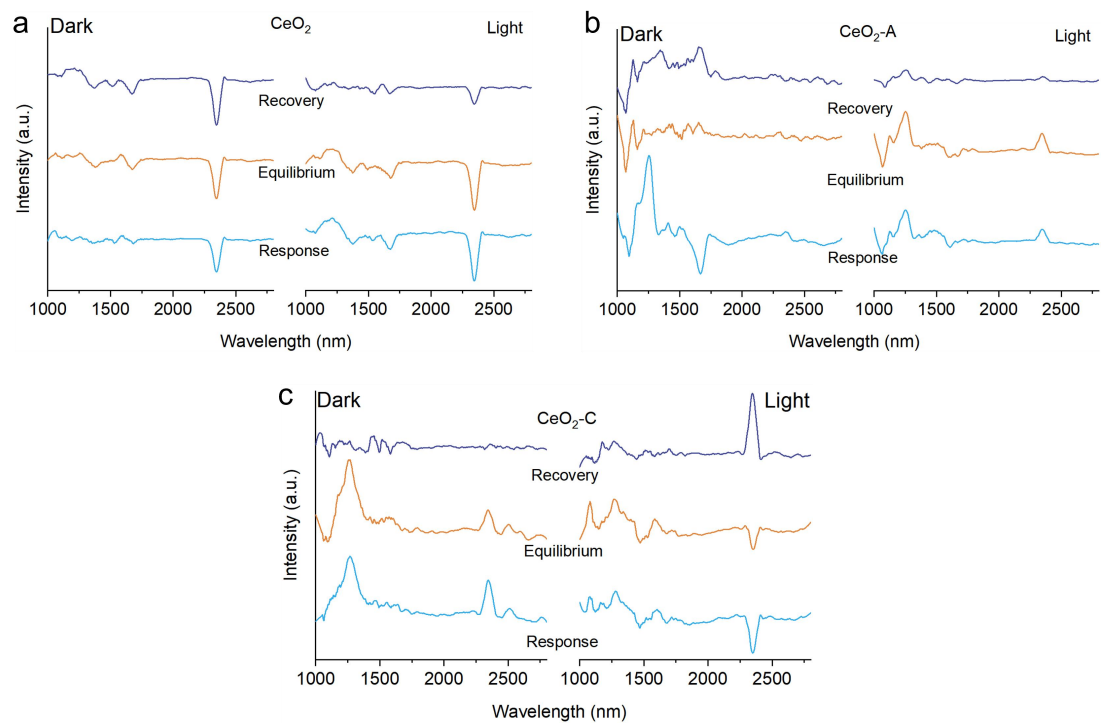
Fig. S29. *In-Situ* FTIR analysis of CeO_2, CeO_2-A and CeO_2-C.